Causes for the Negative Scaling of Extreme Precipitation at High Temperatures

Xiaoming Sun[a] and Guiling Wang[a]

[a] *Department of Civil and Environmental Engineering & Center for Environmental Sciences and Engineering, University of Connecticut, Storrs, CT 06269*

Corresponding author: Dr. Guiling Wang, guiling.wang@uconn.edu

Submitted to Journal of Climate

Submitted: January, 2021; Revised: March, 2022, May 2022

ABSTRACT

Although the intensity of extreme precipitation is predicted to increase with climate warming, at the weather scale precipitation extremes over most of the globe decrease when temperature exceeds a certain threshold, and the spatial extent of this negative scaling is projected to increase as the climate warms. The nature and cause of the negative scaling at high temperature and its implications remain poorly understood. Based on sub-daily data from observations, reanalysis data, and output from a coarse-resolution (~200 km) global model and a fine-resolution (4 km) convection-permitting regional model, we show that the negative scaling is primarily a reflection of high temperature suppressing precipitation over land and storm-induced temperature variation over the ocean. We further identify the high temperature-induced increase of saturation deficit as a critical condition for the negative scaling of extreme precipitation over land. Large saturation deficit reduces precipitation intensity by slowing down the convective updraft condensation rate and accelerating condensate evaporation. The heat-induced suppression of precipitation, both for its mean and extremes, provides one mechanism for the co-occurrence of drought and heatwaves. As the saturation deficit over land is expected to increase in a warmer climate, our results imply a growing prevalence of negative scaling, potentially increasing the frequency of compound drought and heat events. Understanding the physical mechanisms underlying the negative scaling of precipitation at high temperature is, therefore, essential for assessing future risks of extreme events, including not only flood due to extreme precipitation but also drought and heatwaves.

SIGNIFICANCE STATEMENT

Negative scaling, a decrease of extreme precipitation at high local temperature, is a poorly understood phenomenon. It was suggested that the negative scaling may be a reflection of precipitation's influence on temperature. Here we show based on observational data, reanalysis data and climate models that the negative scaling results primarily from the impact of high temperature-induced saturation deficit on precipitation over land and from storm-induced temperature variations over the ocean. In hot weather when moisture is limited (as is over land), large saturation deficit reduces precipitation intensity by slowing down the convective updraft condensation rate and accelerating condensate evaporation, leading to a negative scaling. The same mechanism can also contribute to increased compound drought and heat events.

1. Introduction

As the global climate warms, observational data have shown an increase in the intensity and frequency of extreme precipitation (Fischer and Kutti 2016; Easterling et al. 2017), and this trend is expected to continue (Meehl et al. 2007; Allan and Soden 2008; Kharin et al. 2017; Prein et al. 2017). Because extreme precipitation is intrinsically related to low-level moisture convergence and tends to occur when the atmosphere is close to saturation, its intensity is often proportional to the moisture-holding capacity of the air near the surface of the Earth. Therefore, the Clausius-Clapeyron (C-C) relationship, which dictates the increase with temperature in the capacity of the atmosphere to hold moisture, can be used as a first-order approximation for the scaling of precipitation extremes with warming (Trenberth 1999).

The relationship between extreme precipitation intensity and concurrent local temperature (EPI-T), however, is confounded by several other factors and processes, including atmospheric stability, precipitation efficiency, orographic effect, convective organization, moisture limitation, and latent heat release feedback on storm intensity (e.g., O'Gorman and Schneider 2009; Loriaux et al. 2013; Muller 2013; Singh and O'Gorman 2014; O'Gorman 2015; Dai and Soden 2020). Therefore, it does not, and is not expected to, conform to the C-C scaling (Lenderink and van Meijgaard 2008; Sugiyama et al. 2009; Hardwick Jones et al. 2010; Chen et al. 2011; Utsumi et al. 2011; Mishra et al. 2012; Berg et al. 2013; Prein et al. 2017; Bao et al. 2017; Wang et al. 2017; Da Silva et al. 2020). Specifically, in the context of climate variability and at daily and sub-daily timescales over most of the globe, extreme precipitation increases with local temperature up to a certain threshold, beyond which a lower magnitude of extreme precipitation is associated with higher temperatures. This leads to a peak-shaped relationship curve, with negative scaling at higher temperatures. As the climate warms, both the magnitude of the extreme precipitation peak and the threshold temperature at which extreme precipitation reaches its peak are projected to increase, leading to an upper-rightward shift of the curve relating the two, especially for the increasing branch of the scaling curves (Prein et al. 2017; Wang et al. 2017; Drobinski et al. 2018) (Figure 1). For the descending branch, however, its variation with warming can be more elusive (Drobinski et al. 2018), and the negative scaling is projected to become spatially more widespread in a warmer climate (Wang et al. 2017). Wang et al. (2017) suggested that the C-C scaling is more likely to hold at the peak precipitation intensity (indicated by dots in Figure 1b), since the most intense

precipitation event tends to occur when the atmosphere is close to saturation, a condition conducive to C-C scaling (Wang & Sun, 2022).

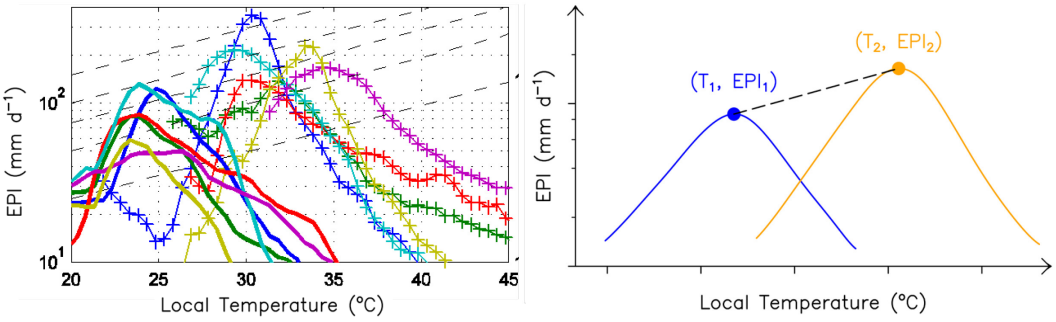

Figure 1. Relationship between extreme precipitation intensity and local temperature (EPI-T). The left panel is based on historical (color solid lines) and projected (color lines with crosses) daily all-season output from six global climate models, using the Indian Monsoon region as an example (from Wang et al. 2017). The right panel is a conceptual diagram illustrating the EPI-T scaling in historical (blue solid line) and future (orange solid line) climates. The black dash lines indicate the Clausius-Clapeyron scaling relationship.

The negative scaling of extreme precipitation at high temperature, although well documented in numerous studies, is poorly understood. Many factors may contribute to it, ranging from artificial effects of the data resolution and the methodology used to analyze the data to true physical mechanisms linking precipitation processes with temperature (e.g., Barbero et al. 2018; Bao et al. 2018; Visser et al., 2021). If higher temperature led to precipitation events that were more intense but spatially or temporally more concentrated (Long et a., 2021), data at coarse resolution would not capture the true response of precipitation intensity to temperature (Utsumi et al. 2011; Wasko et al. 2015; Visser et al., 2021). Mixing data from different seasons might lead to the clustering of large-scale precipitation at low or medium temperature on one end and convective precipitation at high temperature on the other end, which complicates the results (Drobinski et al. 2016; Ali et al. 2018). For physical processes underlying the negative scaling, some have hinted at the possible role of moisture limitation in precipitation at high temperature (Hardwick Jones et al. 2010; Prein et al. 2017; Wang et al. 2017; Wang & Sun, 2022), but this mechanism may not work over oceans, where moisture supply is usually not a limiting factor. Some have pointed to the response of near-surface air temperature to synoptic conditions and precipitation processes, including warming associated with anticyclonic weather systems (Trenberth and Shea 2005; Chan et al. 2016) and cooling during heavy precipitation events (Bao et al. 2017), but this notion is a subject of inconclusive debate (Barbero et al. 2018; Bao et al. 2018). The lack of a consistent relationship

between surface air temperature and atmospheric moisture content may also cause the negative scaling between precipitation extremes and temperature (e.g., Roderick et al. 2019).

Despite the many studies on the relationship between extreme precipitation and temperature, the very nature of the negative scaling is not clearly understood; while not without exception (Visser et al., 2021), comments on the possible causes for negative scaling are often given without direct substantiating evidence. The projected increase in the spatial extent of negative scaling is subject to a similar lack of understanding (Wang et al. 2017). In the current study we aim to establish clear evidence for the negative scaling of extreme precipitation at high temperature, understand the nature of this negative scaling, assess its sensitivity (or the lack of such) to non-physical factors such as spatiotemporal resolution and seasonality, and tackle the physical mechanisms that underlie the negative scaling and its potential implications for future changes. We demonstrate that, for most regions over land at the weather timescale, the intensity of warm-season precipitation extremes decreases at high temperature, and this negative scaling is primarily a reflection of precipitation intensity being suppressed by temperature-induced large saturation deficit. Over oceans except for the subtropical dry zones, negative scaling is also found and results primarily from storm-induced temperature variations stemming from the combined impact of evaporative cooling and cloud radiative effect. As illustrated in Figure 1, the negative scaling at the weather timescale does not contradict the observed and predicted warming-induced increase of extreme precipitation at the climate timescale. The remainder of this article is organized as follows. Section 2 provides a description of the datasets and models used, while Section 3 details the methodologies applied, including the binned scaling analysis and diagnostics related to atmospheric convection. Section 4 presents a thorough examination of the robustness of negative scaling at high temperature, and illustrates the underlying physical mechanisms by exploring the interactions between temperature and precipitation processes, as well as the role of large-scale systems. Conclusions and discussion are given in Section 5.

2. Data and Models

Data from four sources are used in this study. These include the observational Integrated Multi-satellitE Retrievals for Global Precipitation Measurement (IMERG, Final Run version 6, Huffman et al. 2019), the European Centre for Medium-Range Weather Forecasts (ECMWF) fifth generation reanalysis data (ERA5, Hersbach et al. 2020), output from global simulations carried out for this study using the Community Earth System Model (CESM) version 1.2.2.1,

and output from the National Center for Atmospheric Research (NCAR) continental-scale convection-permitting modeling of North America (Liu et al. 2017) using the Weather Research and Forecasting (WRF) model version 3.4.1 (Skamarock et al. 2008).

The half-hourly, 0.1º resolution IMERG is the successor of the Tropical Rainfall Measuring Mission (TRMM) 3B42 precipitation data (Huffman et al. 2007) from the National Aeronautics and Space Administration (NASA). It is an adjusted precipitation product based on estimates from various precipitation-relevant satellite passive microwave sensors comprising the Global Precipitation Measurement (GPM) constellation; it is available for the period June 2000 to near the present and nominally covers the entire globe (primarily for unfrozen surfaces between 60º S and 60º N). The global ERA5 is the successor of ECMWF interim reanalysis (ERA-Interim, Dee et al. 2011) and uses a more advanced assimilation scheme. The ERA5 precipitation at approximately 30 km grid spacing is model simulated and available at every hour from 1950 to near real time; the 2-m air temperature in ERA5 is a reanalysis product that assimilates observed surface air temperature. Also available from ERA5 are dewpoint temperature and surface pressure, which are used to derive the 2-m saturation deficit following the approach of Byrne and O'Gorman (2018). As in Wang et al. (2017), the IMERG precipitation is paired with ERA5 2-m air temperature or 2-m saturation deficit to support the analysis on observed scaling, which we refer to here as "IMERG"; we refer to scaling analysis as "ERA5" if both precipitation and 2-m air temperature or saturation deficit are from ERA5. For comparison purposes, all IMERG and ERA5 analyses are also repeated based on TRMM and ERA-Interim.

The CESM global simulation is performed at *f19* spatial resolution (approximately 1.9º × 2.5º) and over the period 1986-2013 (with the first five years deemed model spin-up), using prescribed sea surface temperature and sea ice fraction according to observations from the Hadley Centre and the National Oceanic and Atmospheric Administration (NOAA) (Hurrell et al. 2008). The atmospheric component is the Community Atmosphere Model, version 5.3 (Neale et al. 2012), with 30 vertical levels; the land component is the Community Land Model 4.5 with satellite phenology (Oleson et al. 2013). To represent present-day climate, the land surface is initialized according to year 2000 conditions (Oleson et al. 2013), and aerosol concentration, CO_2, and other trace gases are all fixed at their year 2000 levels. In addition to daily and 3-hourly model output for the entire simulation period, model output is also saved for every time step (30 minutes) during the five-year period from 1991 to 1995 to examine the sensitivity of extreme precipitation scaling analysis to temporal resolution.

The WRF convection-permitting simulation is conducted at 4-km grid spacing for the contiguous United States (and is referred to as "WRF4km" hereafter), driven with initial and boundary conditions from ERA-Interim for the period October 2000 to September 2013 (Rasmussen and Liu 2017; Liu et al. 2017). In this study, both the hourly and the aggregated 3-hourly and daily WRF4km data are used to examine the sensitivity of the scaling relationship to temporal resolution.

Figure S1 compares the precipitation climatology for the June-July-August (JJA) and December-January-February (DJF) seasons from all four data sources at their native resolution. Both CESM and WRF reproduce the large-scale precipitation climatology reasonably well. Discrepancies in certain regions can be large, especially for CESM. Precipitation during DJF, for example, is strongly underestimated by CESM over the Amazon basin, a common global model deficiency also found in other studies (e.g., Zhang et al. 2017). Moreover, CESM also captures the global pattern of extreme precipitation in comparison with IMERG and ERA5, although the magnitude is much lower as expected from coarse-resolution (~200 km) simulations (not shown).

3. Methods

Using data from each of the four sources respectively, we identify and track the extreme precipitation events under different temperatures, and analyze how extreme precipitation scales with temperature and other variables (e.g., saturation deficit) at different lead/lag times. For CESM, additional diagnostics related to precipitation and convection are examined to further understand the physical processes underlying the negative scaling of precipitation extremes at high temperature. In addition to global analysis, 16 sample regions (Figure S2) over land and ocean spanning the tropics and extratropics are chosen for more detailed analysis. Due to computational constraint, especially for event tracking, we aggregate the half-hourly IMERG, hourly ERA5 and hourly NCAR WRF model output as 3-hourly data for most of the analysis. In section 4a, we demonstrate that this treatment does not impact the results because the sensitivity to temporal resolution is minimal as also found in previous studies (e.g., Drobinski et al. 2018). It should be noted that the focus of this study is on extreme precipitation scaling with temperature and therefore the surface air temperature is used as the covariate of precipitation intensity. Some past studies used dewpoint temperature as the precipitation covariate (see Fowler et al. 2021 for a comprehensive review). However, since dewpoint is a measure of specific humidity, it is not suitable for this study.

196 *a. Binned scaling analysis*

197 Our primary EPI-T scaling analysis is based on sub-daily data and conditional on near-
198 surface air temperature (taken as local 2-m air temperature), following the approach of Wang
199 et al. (2017). Rather than using daily averaged temperature and sub-daily precipitation to
200 reduce the imminent impact of precipitation on temperature as in Drobinski et al. (2018) and
201 Da Silva et al. (2020), we analyze both temperature and precipitation at the sub-daily timescale
202 to explore their interactions. This choice is also necessitated by our event tracking and lead-lag
203 analysis that require sub-daily data. Specifically, all sub-daily precipitation data in each
204 specific area within the analysis period are first binned according to the corresponding near-
205 surface air temperature, and a bin size of 0.5° C is used. For each temperature bin, the 99th
206 percentile of precipitation is identified, and the extreme intensity is then defined as the average
207 of precipitation rates that exceed the 99th percentile within the bin, and the corresponding near-
208 surface air temperatures are averaged to represent the bin temperature. Temperature bins with
209 fewer than 1,000 data points, typically found at the lowest and highest ends of local temperature
210 variations, are discarded. The resulting precipitation extremes are smoothed (using a three-bin
211 moving average) to characterize the scaling relationship between precipitation extremes and
212 near-surface air temperature, and to identify the temperature at which extreme precipitation
213 peaks, denoted as T_{peak}. A similar binned analysis is also conducted to derive the relationship
214 between sub-daily precipitation and near-surface saturation deficit (EPI-SD), using a bin size
215 of 0.5 g kg^{-1}.

216 For all precipitation events underlying each "extreme" data point within each temperature
217 bin, we then track the temporal variation of precipitation, temperature, and some convection-
218 related variables to assess the timing and magnitude of changes of temperature (and other
219 variables) during storm development. This analysis enables us to evaluate whether the
220 temperature differences between storm events in different bins are already present before storm
221 development or caused by the storm, and to quantify how much of the difference can be
222 attributed to the storm.

223 The aforementioned analyses are conducted globally and for each of the 16 representative
224 regions as well. The global analysis is not based on each individual grid cell; instead, data from
225 25 grid cells centering around each grid cell is pooled together to increase the sample size in
226 the extreme analysis. To compare data from the four different sources, the scaling analyses are
227 conducted over their common period, December 2000 to August 2013, focusing on the warm

season (JJA for the Northern Hemisphere and DJF for the Southern Hemisphere) when convective precipitation is dominant. Because of differences in spatial resolution, the number of grid cells needed to cover a specific representative region can differ dramatically across different datasets. To ensure similar spatial coverage for each region across all datasets, some resampling is necessary. For study regions within the contiguous United States, we resample IMERG, ERA5, and WRF4km to a 64-km resolution on the WRF grid (WRF64km-G or simply WRF). For regions outside the contiguous United States, we resample the IMERG precipitation to the ERA5 grid. To preserve the characteristics of precipitation extremes, no spatial interpolation is conducted; instead, resampling simply takes the raw data from the closest grid point. Overall, 169 (13 × 13) grid cells from WRF64km-G and 1089 (33 × 33) grid cells from ERA5 occupy an area similar to that of 25 (5 × 5) grid cells from CESM (Figure S2). Subject to computer memory constraint, the ERA5 grid has to be resampled at every other grid point before conducting scaling analysis. This leads to a total of 289 (17 × 17) grid cells that are eventually used for the scaling analysis based on the ERA5 grid. As is evident from Figures S3 and S4, the details of the resampling process do not influence the qualitative scaling behavior of precipitation extremes. This result is consistent with Drobinski et al. (2018), showing minimal sensitivity of EPI-T scaling to spatial resolution.

b. Atmospheric convection diagnostics

To explore the physical processes underlying the negative scaling of precipitation extremes at high temperature, we analyze diagnostics directly related to atmospheric convection, including the cumulus updraft condensation rate, cumulus downdraft evaporation rate, and downdraft convective available potential energy. Limited by the availability of data for the needed variables, the diagnostics described here are based on CESM output only.

Following Houze et al. (1980), we estimate cumulus updraft condensation rate C_u and cumulus downdraft evaporation rate E_d as

$$C_u = \int_{z_B}^{z_T} M_u \left[\lambda_u \left(r_e - r_u \right) - \frac{dr_u}{dz} \right] dz \tag{1}$$

$$E_d = \int_{z_B}^{z_T} M_d \left[\lambda_d \left(r_e - r_d \right) + \frac{dr_d}{dz} \right] dz , \tag{2}$$

where z is height, z_B (z_T) is cloud base (top) height, M_u (M_d) is updraft (downdraft) mass flux, λ_u (λ_d) stands for updraft (downdraft) entrainment rate, and r_e, r_u, and r_d are environment, updraft, and downdraft water vapor mixing ratio, respectively. Among the variables needed for the calculation of C_u and E_d, four – M_u, M_d, λ_u, and λ_d – are directly obtained from the cumulus parameterization (Zhang and McFarlane 1995) of CESM, while z_B and z_T can be determined from the vertical profiles of M_u and M_d. We take the grid value of water vapor mixing ratio as r_e and estimate r_u and r_d as the saturation mixing ratio at the environmental temperature and pressure.

The downdraft convective available potential energy (DCAPE) for an air parcel can be estimated as

$$DCAPE = \int_{p_i}^{p_n} R_d \left(T_{\rho e} - T_{\rho p} \right) d \ln p \,, \tag{3}$$

where p is atmospheric pressure, p_i is the pressure from which the parcel starts to descend, p_n is surface pressure or the pressure where a descending parcel achieves neutral buoyancy (whichever is smaller), R_d is the gas constant for dry air, and $T_{\rho e}$ and $T_{\rho p}$ are the density temperature of the environment and air parcel, respectively (Emanuel 1994). Because the maximum kinetic energy that a descending parcel can achieve is proportional to DCAPE, DCAPE can be used as an indicator of maximum downdraft strength within storms: the higher the value of DCAPE, the stronger the downdraft could potentially be. DCAPE for each temperature bin is estimated using the average air temperature and water vapor mixing ratio corresponding to the extreme precipitation rates in that temperature bin. We adapt the DCAPE calculation from Emanuel (1994), which eliminates the need for total water mixing ratio information by assuming that the parcel is cooled isobarically through a wet-bulb process before descending pseudo-adiabatically with just enough evaporation to keep it saturated. DCAPE, as an indicator of maximum downdraft when precipitation supply is sufficient and background wind shear is absent, is not a direct measure of the actual downdraft strength. However, its response to temperature variation is consistent with that of the estimated cumulus downdraft evaporation rate E_d (as shown later in the Results section), lending confidence to the accuracy of both diagnostics and their relevance as a metric for downdraft strength.

4. Results

a. The robustness of the negative EPI-T scaling

For the EPI-T relationship based on data from all seasons, the negative scaling at high temperature is dominated by precipitation events from the warm season (which coincides with the wet season in many regions) (Wang et al. 2017). Lumping data from warm and cold seasons together mixes convective and large-scale precipitation regimes, which may lead to an artificial negative scaling that does not reflect a true physical process relating extreme precipitation to temperature. We therefore focus on the warm season only, when convective precipitation is abundant and dominant. The 16 regions in Figure S2 are used to sample different climate regimes in the tropics and extratropics.

Figure 2 compares the EPI-T relationship for the 16 sample areas using sub-daily data from all four sources during their overlapping period (2001-2013). The magnitude of precipitation extremes differs remarkably among the four sources and generally increases as the native resolution of the data becomes finer from CESM to ERA5 to IMERG and WRF. Relative to the observational reference IMERG, CESM substantially underestimates the intensity of extreme precipitation at sub-daily timescales, while WRF overestimates the extreme precipitation intensity compared with ERA5, which shows an overall agreement with IMERG (solid lines in Figure 2). Despite these rather substantial differences among the four data sources in the magnitude of precipitation extremes, and despite the vastly varying climate regimes of the 16 sample regions, the EPI-T relationships derived from all data sources for all sample regions are qualitatively similar and feature a negative scaling at high temperature (solid lines in Figure 2). The increasing branch of the scaling curves at lower temperatures can be minimal or even absent because the near-surface air temperature during the warm season is mostly above the threshold temperature at which the extreme precipitation peaks (T_{peak}). The increasing branch would be more prominent and dominated by winter precipitation if the scaling curves were derived using data from all seasons (e.g., Wang et al. 2017).

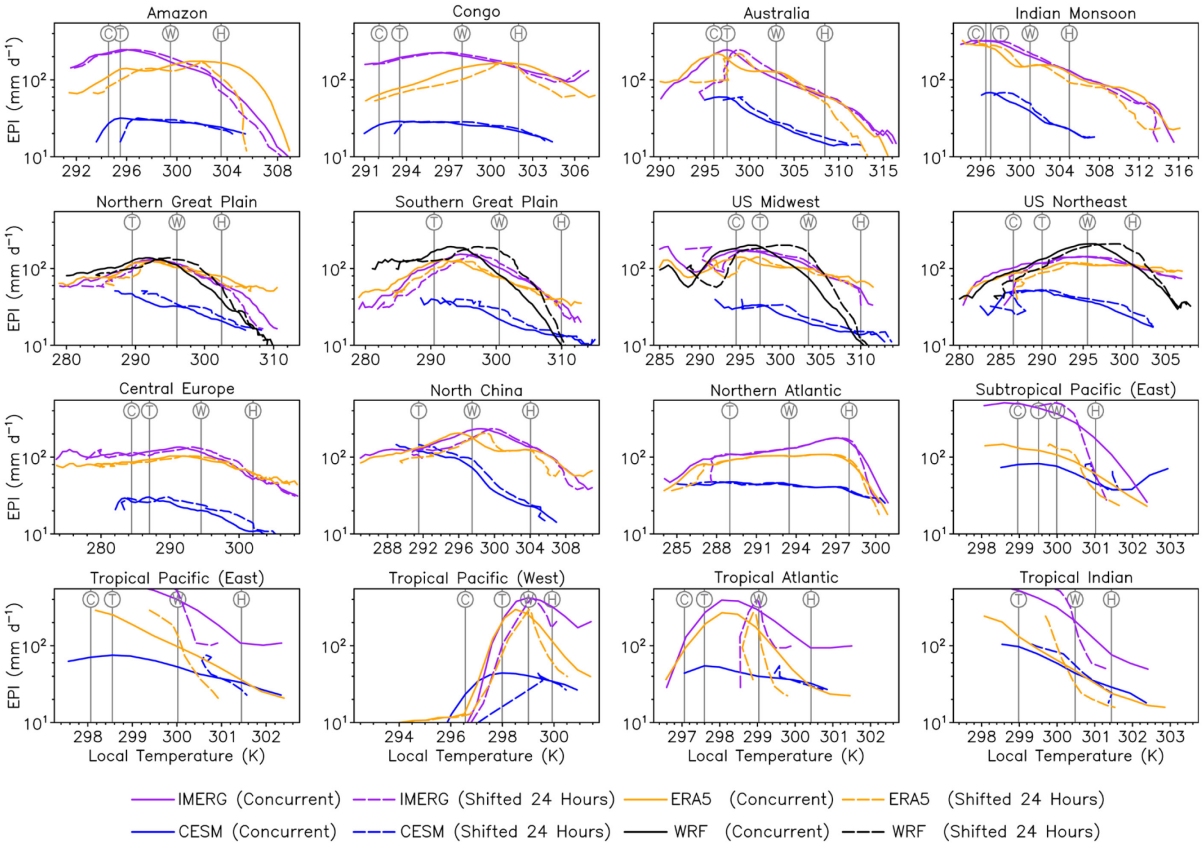

Figure 2. The EPI-T scaling relationship that links extreme precipitation intensity to concurrent near-surface air temperature (solid lines) and antecedent near-surface air temperature (dashed lines) for 16 sample areas. The analyses are based on 3-hourly data from IMERG, ERA5, CESM, and WRF during the 2001-2013 warm seasons, with temperature in K and EPI in mm day^{-1}. The dashed lines are based on the same extreme precipitation data as the solid lines but with temperature shifted to the values 24 hours ahead of precipitation. The vertical gray lines indicate the temperature bins used for more detailed analysis, including a cold bin (C, only for areas where the EPI-T curve in CESM includes an increasing branch), a threshold bin (T, which corresponds to the largest magnitude of extreme precipitation in CESM), a warm bin (W), and a hot bin (H).

Since extreme precipitation decreases when the surface air temperature exceeds T_{peak}, we use the percentile of T_{peak} as an indicator for how common or how rare the conditions are inducive to negative scaling. Figure 3 shows the global pattern of T_{peak} percentile based on warm season local temperature statistics, where a lower percentile for T_{peak} means more common or more frequent occurrence of negative scaling. It is clear from Figure 3 that negative scaling is detected over most land areas; relative to IMERG, ERA5 and WRF, the coarse-resolution global model CESM generally overestimates the frequency of conditions under which negative scaling occurs. For example, over most of the U.S., T_{peak} is at or lower than the 5th percentile of warm-season temperature in CESM, but ranges from less than 5th percentile to over 60th percentile in IMERG, ERA5 and WRF. However, the overall spatial patterns of T_{peak}

percentile from different data sources show a remarkable agreement, all indicating that negative scaling is a common warm-season phenomenon over most land areas and in much of the tropical oceans. Over the unshaded areas in Figure 3, negative scaling is either extremely rare or not detected. Data from different sources are consistent in identifying such areas, including the subtropical dry zones over the oceans and high-latitude oceans with no real warm season.

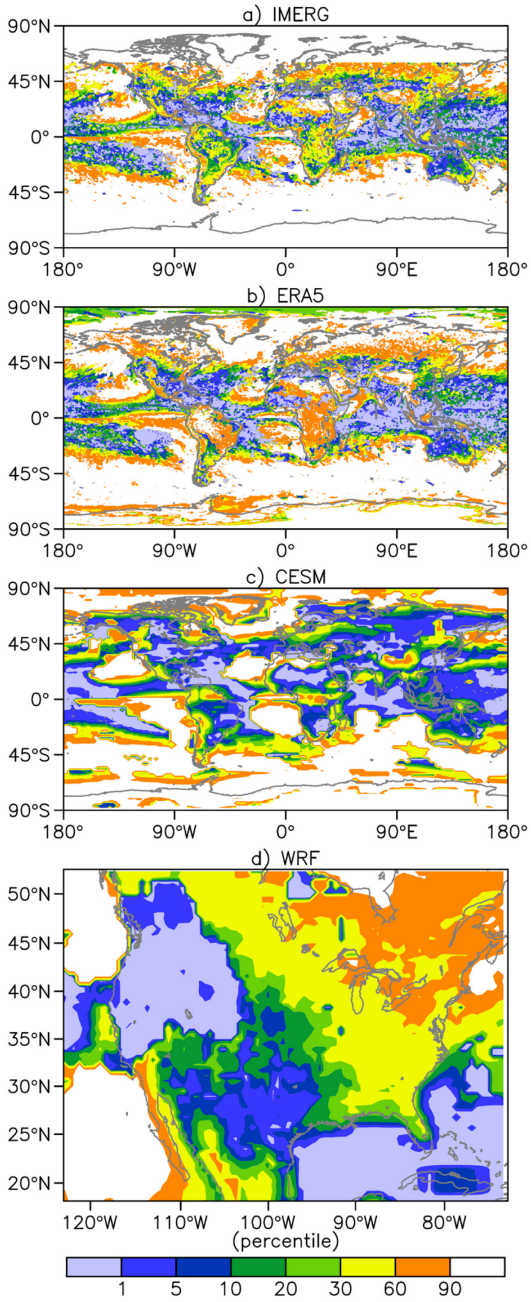

Figure 3. Percentile of T_{peak} at which extreme precipitation reaches its maximum value in the EPI-T scaling curve. These percentiles are based on 3-hourly data from (a) IMERG, (b) ERA5, (c) CESM, and (d) WRF during the 2001-2013 warm seasons. At each grid point, data from its surrounding 25 grid cells are used. Lower percentiles of T_{peak} indicate more common occurrence of negative scaling.

The negative EPI-T scaling relationship is robust against the data temporal and spatial resolutions. As the temporal resolution changes from sub-hourly to hourly, three-hourly, and daily, the intensity of the precipitation extremes from all four data sources decreases, but qualitatively, the overall EPI-T relationship does not change (Figure 4 using the U.S. Southern Great Plain as an example; see Supplementary Figure S5 for all 16 sample areas). Negative scaling at high temperature is clearly present in all sample areas at all temporal resolutions examined, consistent with Drobinski et al. (2018, their Fig. 2). Quantitatively, the magnitude of the negative scaling rate generally decreases as the temporal resolution becomes finer. This is especially obvious in CESM for the tropical wet climates (e.g., in the Amazon and Congo), where the EPI-T curve for daily data shows a clear negative scaling while the curve based on 30-minute resolution is almost flat. Similar to the effect of temporal accumulation, spatial aggregation from fine to coarser grids (through averaging) reduces the magnitude of the extreme precipitation, but does not qualitatively change the EPI-T relationship (results not shown), in agreement with Drobinski et al. (2018). Moreover, the EPI-T relationship also shows minimal sensitivity to spatial resampling to various resolutions that takes the nearest neighbor value in the scaling analysis. Resampling the IMERG data from 0.1° to 0.3°, for example, or resampling the WRF output from 4km to 64km grid spacing causes negligible change in the derived EPI-T relationship corresponding to each data source (Figures S3-S4).

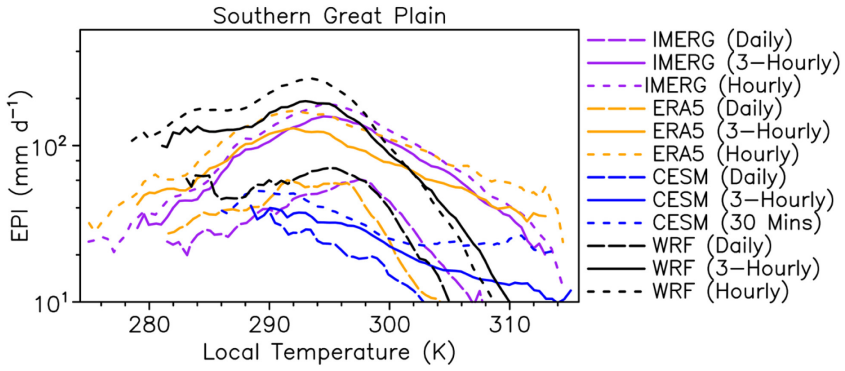

Figure 4. Sensitivity of the EPI-T scaling to temporal resolution, using the Southern Great Plain sample area as an example. The scaling curves are derived from daily (dashed lines), 3-hourly (solid lines), and hourly or 30-minute (dotted lines) data from IMERG (purple), ERA5 (orange), CESM (blue) and WRF (black), with temperature in K and EPI in mm day^{-1}. The results are for the warm seasons of 2001-2013, except for the CESM-based 30-minute scaling analysis that is based on the warm seasons of 1991-1995 (limited by the availability of the 30-minute time-step output).

b. Impact of precipitation process on temperature

To assess the impact of precipitation and its associated weather systems on near-surface air temperature, we track all individual storm events underlying the identified "extremes" within each temperature bin to examine how temperature and other variables evolve during a storm's lifetime. In this "storm tracking" analysis, we apply a 24-hour moving average to all time series to remove the diurnal cycle and focus on storm-induced variations. For most regions, near-surface air in the warm and hot bins generally experiences slight cooling (or even warming) before the time of the storm peak, while near-surface air in the cold and threshold bins experiences stronger cooling. Most of the temperature changes occur within the 24 hours before the storm peak, as shown in Figure 5 using the U.S. Southern Great Plain as an example. Results for all sample regions are presented in supplementary Figures S6-S9 for IMERG, ERA5, CESM, and WRF, respectively. This cooling is closely related to cloud radiative effects that are the strongest within 24 hours before and after the storm peak (as evident from the surface insolation plot in Figure S10 using CESM as an example). In CESM for most sample areas, cloud content is much higher during storm events in the cold and threshold bins than those in the warmer bins, and the transition from predominantly low-level clouds to medium- and high-level clouds (reflecting the transition from shallow to medium and deep convection) occurs within one day before the storm peak (Figures S11-S12). The other cooling process, through evaporation of rain droplets in the lower troposphere and water at the surface, occurs more imminently to the precipitating process. Therefore, one day before the storm peak is sufficient to capture most of the storm's impact on temperature; earlier temperature differences between bins reflect variations not directly related to the imminent storm events.

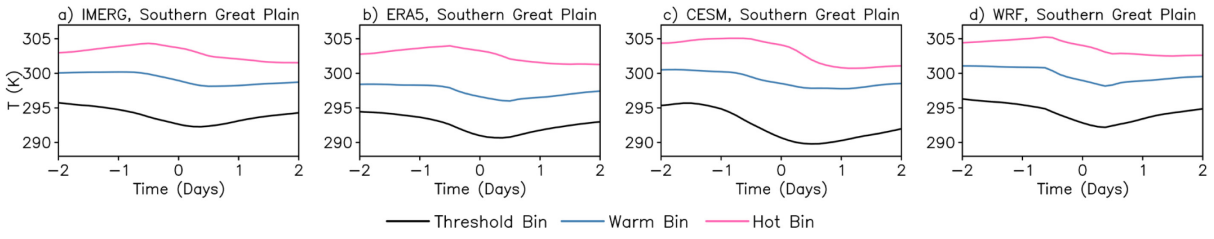

Figure 5. Evolution of near-surface air temperature, using the Southern Great Plain sample area as an example. These are time series of near-surface air temperature (K) before and after the peak of storm derived among the extreme events within each temperature bin, based on 3-hourly data from (a) IMERG, (b) ERA5, (c) CESM, and (d) WRF during the 2001-2013 warm seasons. Time zero is when precipitation peaks during each storm event, with a negative value on the x-axis denoting the time before the storm peak and positive after. The threshold, warm and hot bins are as marked in Figure 2.

In most land areas, the range of temperature variation in the absence of storm events is large (as reflected by the distance between lines at -1 day in Figure 5 and Figures S6-S9), and

the bin-to-bin temperature difference at the storm peak results from the combination of storm-free temperature variations and storm-induced temperature changes. Based on data from all four sources, over most of the land regions examined, less than 25% of the temperature differences at the storm peak between the cold (or threshold) and hot bins are attributable to the storm-induced temperature changes (Figure 6). Over most oceanic areas sampled, temperature variation in the absence of storm events is small or negligible as indicated by the small temperature difference across different temperature bins one day ahead of the storm events (e.g., in the subtropical Pacific (East), Figures S6-S9); and storm-induced temperature change generally accounts for over 60% of the differences between temperature bins (Figure 6). So the impact of precipitation process (or the lack of it) on temperature plays an essential role in shaping the EPI-T relationship over oceans. While results from the four data sources show some quantitative differences, they are remarkably similar in terms of the clear contrast between land and ocean, with a substantially higher fraction of temperature differences attributable to storm-induced variations over oceans than over land.

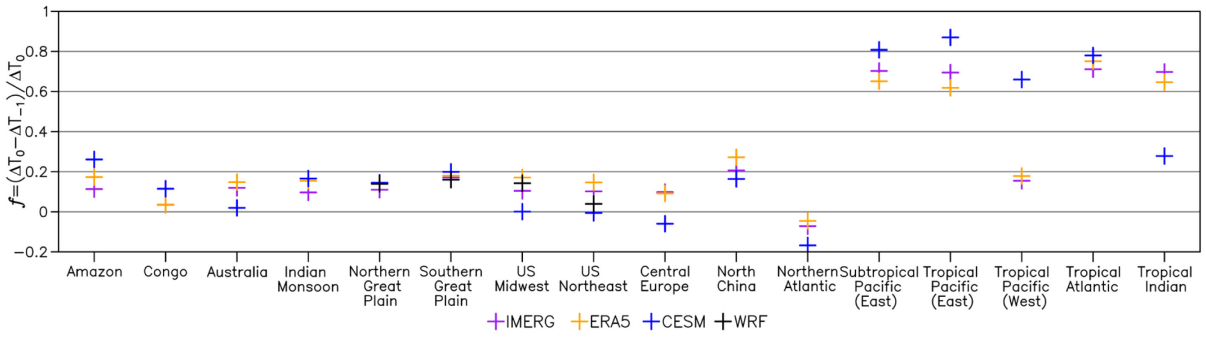

Figure 6. The fraction of temperature difference between the cold (or threshold) and hot bins attributable to storm-induced temperature change, for 16 sample areas based on four data sources during the 2001-2013 warm seasons. The fraction was calculated as $f = (\Delta T_0 - \Delta T_{-1}) / \Delta T_0$, where ΔT_0 represents the temperature difference between the cold (or threshold) and hot bins at time zero (i.e., at the peak of the storm events), and ΔT_{-1} at one day (24 hours) ahead.

The storm's impact on near-surface air temperature has been emphasized in previous studies focusing on the negative scaling of extreme precipitation. In general, heavier precipitation tends to produce stronger evaporative cooling, and this cooling unavoidably would shift the events toward lower temperature bins (Bao et al. 2017). To eliminate the impact of storm-induced temperature change, we adjust the EPI-T curve in Figure 2 by shifting extreme precipitation data to a bin pertaining to the temperature 24 hours before the storms' peak; this results in the dashed lines in Figure 2. For most areas over land, even though using

the antecedent temperature does shift extreme events among temperature bins, the adjusted EPI-T curve (with storm-induced cooling or warming removed; dashed lines in Figure 2) retains the general shape of the original, with a negative scaling at high temperature. Differences between the original and adjusted curves are more substantial over oceanic areas. This further confirms that storm-induced temperature change is not the primary cause of the negative scaling over land, although it plays an important role over oceans. This strong contrast between land and ocean might be due to the abundance of low-level clouds over oceans during the development of heavy storms (Figures S11-S12), which tends to produce an overall cooling effect. In combination with evaporative cooling, the impact of precipitation process on near-surface air temperature is thus amplified over the ocean.

c. Impact of temperature on precipitation and possible mechanisms

To assess the impact of temperature on precipitation, we analyze the lagged EPI-T relationship on various sub-daily timescales, with near-surface air temperature leading precipitation by up to 18 hours to reduce or eliminate the impact of precipitation process on temperature. As the lead time increases from zero to 18 hours, the presence of negative scaling at high temperature and the general shape of the scaling curve are qualitatively preserved for all regions. This holds regardless of whether data from IMERG, ERA5, CESM, or WRF are used (Figure 7 using the U.S. Southern Great Plain as an example; results for all 16 sample areas in Supplementary Figures S13-S16). These results, together with the high degree of similarity between the solid and dashed curves in Figure 2, suggest that temperature's impact on precipitation plays an important role in the negative scaling of precipitation extremes at high temperature.

In Figure 7 and Supplementary Figures S13-S16, as the lead time increases, the curves shift and the corresponding T_{peak} values change accordingly. Over most land areas and relative to the scaling curve with lead time zero, the deviation generally increases with lead time in CESM, but increases and then decreases with lead time in IMERG, ERA5 and WRF. Based on data at the sub-daily resolution, the scaling curve (especially T_{peak}) is influenced by the diurnal cycle of temperature. If heavy precipitation tends to occur at a certain time of the day (e.g., in IMERG, ERA5 and WRF), the scaling curve will shift away from the concurrent curve as the lead time increases from zero and shift back towards the concurrent curve when the lead time approaches 24 hours. This does not occur in CESM, indicating that heavy precipitation might not have a clear "preferred time" in the coarse-resolution CESM simulation.

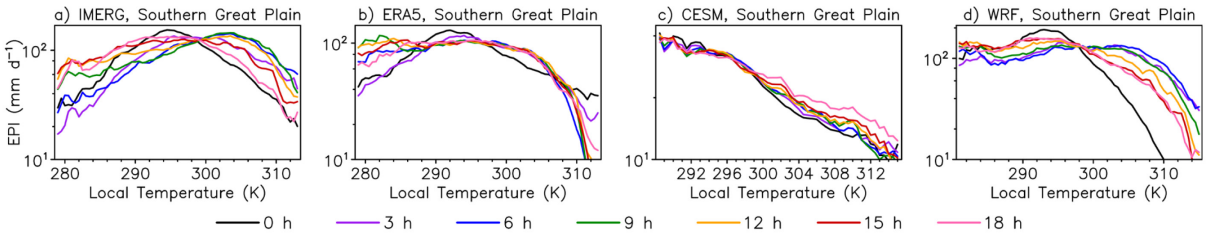

459

460 **Figure 7.** The EPI-T scaling relationship, with temperature (K) leading precipitation (mm
461 day^{-1}) by up to 18 hours, for the Southern Great Plain sample area. These relationships are
462 based on 3-hourly data from (a) IMERG, (b) ERA5, (c) CESM, and (d) WRF during the 2001-
463 2013 warm seasons.

464 Based on the comparison of the CESM results with those from IMERG and ERA5 (Figures
465 2-7), it is evident that, although CESM does underestimate the T_{peak} percentile, it is capable of
466 capturing the negative scaling of extreme precipitation at high temperature. We therefore make
467 use of CESM to study atmospheric convection under high temperature. At the process level,
468 the decrease in extreme precipitation at high temperature in CESM is dominated by a decrease
469 in the cumulus updraft condensation rate, with a minor contribution from enhanced evaporation
470 in the atmosphere (Figure 8). Consistent with observational studies (Berg et al. 2013), in the
471 high temperature range, the CESM-simulated extreme precipitation (gray lines in Figure 8) is
472 primarily from cumulus convection (black lines), and the decrease in extreme precipitation at
473 high temperature is dominantly a decrease in extreme convective precipitation with
474 temperature. The convective precipitation relationship with temperature closely tracks the
475 cumulus updraft condensation rate (blue lines), which increases with temperature and then
476 decreases or levels off as temperature exceeds a certain threshold. Meanwhile, the cumulus
477 downdraft evaporation rate (magenta lines), albeit small in magnitude, either increases with
478 temperature or decreases more slowly than precipitation in most selected areas. This is
479 consistent with the column maximum downdraft convective available potential energy
480 (DCAPE) that peaks at high temperature (Figure S17). As large DCAPE tends to produce
481 strong downdrafts that bring drier air from upper levels, evaporation tends to be stronger when
482 temperature is high. Adding the downdraft evaporation back to extreme precipitation leads to
483 a scaling curve (black dashed lines) with a flattened descending branch (relative to the EPI-T
484 scaling curve) but is insufficient to qualitatively change the nature of the scaling. These results
485 indicate that the slowing down of cumulus updraft condensation rate at high temperature is the
486 dominant process underlying the negative scaling of extreme precipitation in CESM.

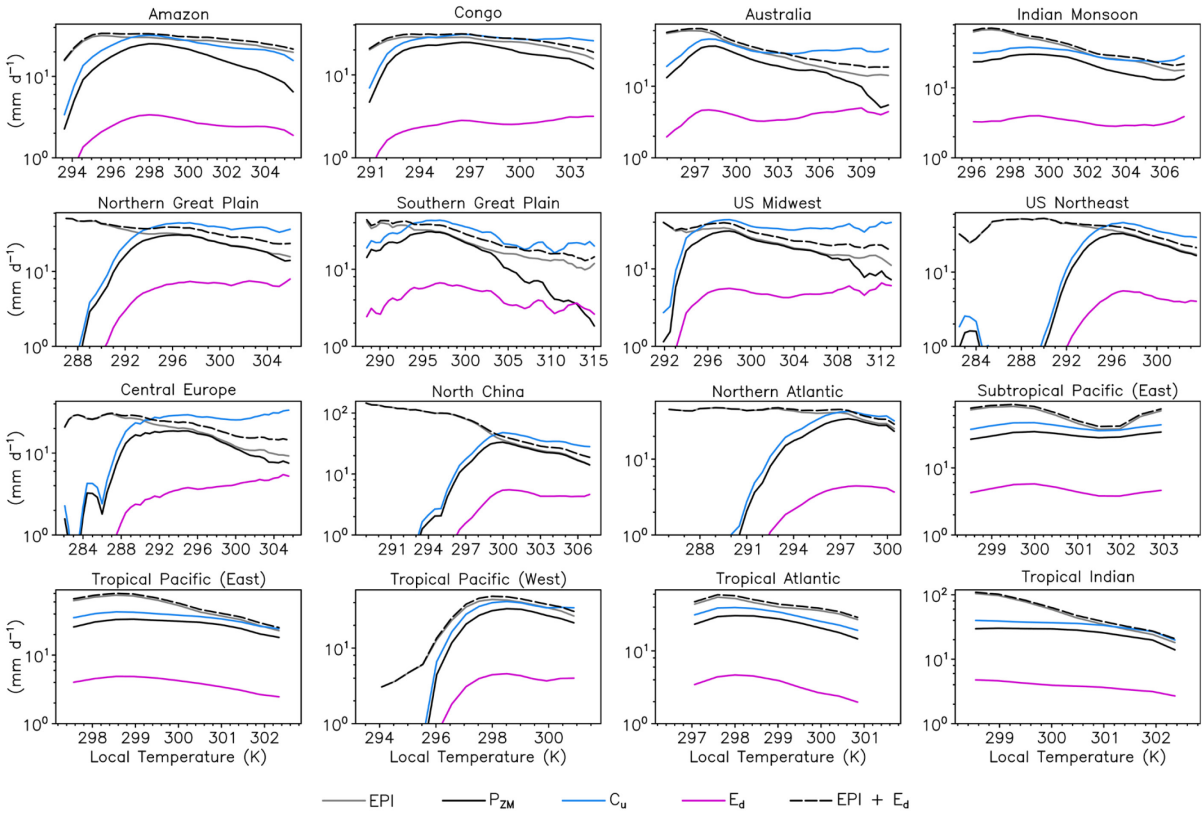

487

488 **Figure 8.** Moisture flux (mm day^{-1}) variation with temperature (K) during extreme
489 precipitation events, based on 3-hourly CESM output during the 2001-2013 warm seasons for
490 16 sample areas. The moisture fluxes plotted include extreme precipitation intensity EPI (gray
491 lines) and the corresponding convective precipitation P_{ZM} (black solid lines), updraft
492 condensation rate C_u (light blue lines), downdraft evaporation rate E_d (magenta lines) and
493 $\mathrm{EPI} + E_d$ (black dashed lines).

494 Further inspection of the cumulus updraft condensation rate reveals that its variation is
495 primarily associated with variations in convective motion: the contribution of saturated ascent
496 to condensation rate (2nd term of Eq. 1 in section 3b) is one order of magnitude greater than
497 the direct impact of mixing dry air from the environment (1st term of Eq. 1 in section 3b)
498 (results not shown). This suggests that the negative scaling is due to suppression of convection
499 at high temperature. Compared with the cold and threshold bins, where the entire air column is
500 close to saturation in all 16 sample regions, the atmosphere in the warm and hot bins features
501 greater saturation deficit (Figure S18). As convective updraft is typically saturated, the
502 entrained air with greater saturation deficit at high temperature tends to deplete cloud buoyancy
503 more efficiently (Brown and Zhang 1997; Redelsperger et al. 2002; Derbyshire et al. 2004;
504 Takayabu et al. 2010). Moreover, as in high-resolution simulations (Romps 2010), in our study
505 the updraft entrainment rate in CESM is also strong for weak convective activities at high

506 temperature (Figures S19-S20). Therefore, the enhanced saturation deficit is an important cause
507 for the suppressed convection (consequently, negative scaling) at high temperature in CESM.

508 Atmospheric saturation deficit (SD) can be quantified using the difference between the
509 saturation water vapor mixing ratio (r^*) and the actual water vapor mixing ratio (r):
510 $\mathrm{SD} = r^* - r$, where r^* depends solely on temperature at a given pressure following the C-C
511 equation, while r is influenced by surface evaporation, large-scale advection, convection, and
512 microphysical processes. The SD difference between the threshold temperature bin ("a") and a
513 warmer bin ("b") can be written as the sum of two terms, one ($\Delta\mathrm{SD}_1 = r_b^* - r_a^*$) determined by
514 temperature differences and the other ($\Delta\mathrm{SD}_2 = r_a - r_b$) reflecting differences in water vapor
515 mixing ratio. Figure 9 shows the vertical profile of $\Delta\mathrm{SD}$ in CESM and the contribution of its
516 two components using four sample regions as examples; results for other regions are similar
517 (Figure S21). Across the whole vertical profile of the atmosphere, SD increases from the
518 threshold bin to warm (blue lines in Figures 9 and S21) and hot bins (pink lines in Figures 9
519 and S21), and this increase is dominated by the temperature-controlled term (dotted lines)
520 below ~600 hPa. Compared with the threshold bin, storm events in the warm and hot bins
521 generally feature more water vapor in the lower troposphere, which tends to reduce the
522 saturation deficit (i.e., $\Delta\mathrm{SD}_2$ is negative, dashed lines); the magnitude of this decrease,
523 however, cannot offset the large increase induced by higher temperature (i.e., $\Delta\mathrm{SD}_1$, dotted
524 lines). At upper levels, the comparison is more complex, as temperature differences between
525 different bins might not be consistent with the near-surface air temperature differences. The
526 results in Figures 9 and S21 are consistent with the notion that r generally increases with
527 temperature more slowly than r^* does due to moisture limitation (Sherwood and Fu 2014).

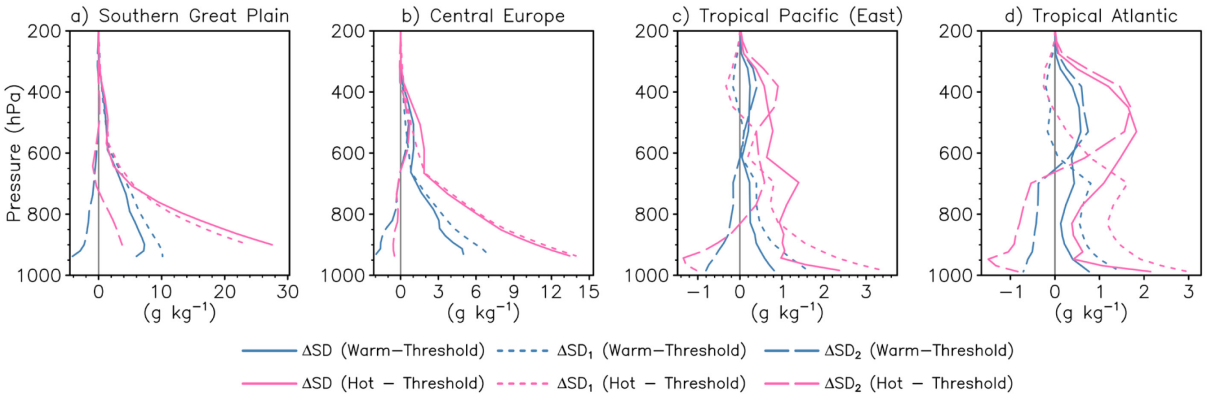

528

529 **Figure 9.** Updraft saturation deficit (g kg^{-1}) comparison across selected temperature bins
530 in four sample areas: (a) Southern Great Plain, (b) Central Europe, (c) Tropical Pacific (East),
531 and (d) Tropical Atlantic. Vertical profiles of updraft saturation deficit difference ΔSD
532 between the threshold bin and the warm (cyan solid lines) or hot (pink solid lines) bin are based
533 on warm-season 3-hourly CESM output during the 2001-2013 warm seasons. Also shown are
534 the contributions from temperature difference ΔSD_1 (dotted lines) and from water vapor
535 mixing ratio difference ΔSD_2 (dashed lines).

536 Based on results from our analysis of extreme precipitation binned according to near-
537 surface saturation deficit, extreme precipitation decreases monotonically as the saturation
538 deficit increases over land (Figure 10). Over the ocean, a similar trend is found at relatively
539 large saturation deficit, with some exceptions in the northern Atlantic and tropical Pacific
540 (West) in IMERG and ERA5 when the atmosphere is close to saturation. Relative to the land
541 areas, saturation deficit is much smaller over oceans due to the abundant moisture supply from
542 the surface, with a sharp contrast of extreme precipitation over a small range of saturation
543 deficit. Similar to temperature variation over oceans being dominated by storm-induced
544 temperature change, the relationships in Figure 10 over the ocean are possibly a result of
545 descending motion that brings dry air from aloft, which is to be further examined in Section
546 4d. This is consistent with the fact that the saturation deficit profiles over oceans are rather
547 homogeneous across the low- and mid-troposphere (Figure S18). Over land, due to limited
548 moisture supply and higher temperature, saturation deficit is large in the lower troposphere
549 below ~600 hPa and rapidly diminishes with altitude.

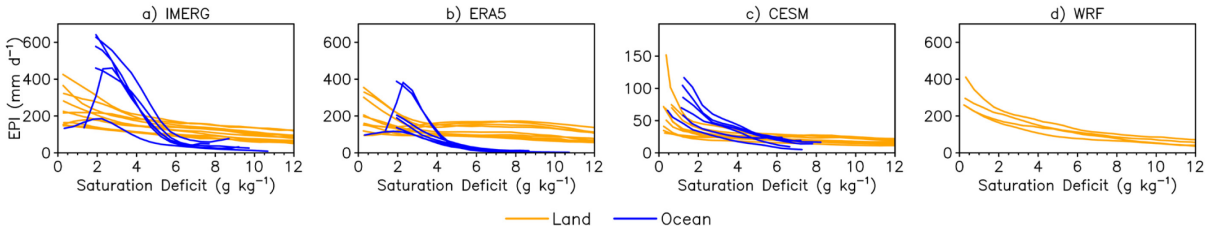

Figure 10. Scaling of extreme precipitation (mm day^{-1}) with near-surface saturation deficit (g kg^{-1}) (EPI-SD). The relationships are based on 3-hourly data from (a) IMERG, (b) ERA5, (c) CESM, and (d) WRF during the warm seasons of 2001-2013. The blue lines are for six oceanic sample areas and the orange lines are for the ten land sample areas shown in Figure S2.

On the other hand, the impact of precipitation process (or the lack of it) on saturation deficit might also contribute to the relationship curves in Figure 10, including for example moistening by evaporation of rain and drying due to subsidence. These effects, however, are important over oceans only and are not the dominant process underlying the relationship shown in Figure 10 over land. This is confirmed through tracking the near-surface saturation deficit prior to and during extreme precipitation events (Figures 11 and S22-S25). Over most land areas, the near-surface saturation deficit contrasts among different temperature bins already exist prior to the development of storm events, and precipitation processes modify the saturation deficit differences only slightly (Figures 11 and S22-S25). This is a strong indication that the relationship shown in Figure 10 for the land areas is a result of saturation deficit influencing extreme precipitation, not the other way around. Over the ocean, however, the near-surface saturation deficit is similar among the various temperature bins prior to the storm events, and differences among the bins develop during and after the storm events. The relationship shown in Figures 10 and 11 for oceanic areas is therefore a reflection of temperature (and saturation deficit) responding to precipitation process over the ocean. This notion is further corroborated by the breakdown of a monotonic relationship between saturation deficit and extreme precipitation in the northern Atlantic and tropical Pacific (West) in IMERG and ERA5 (Figure 10).

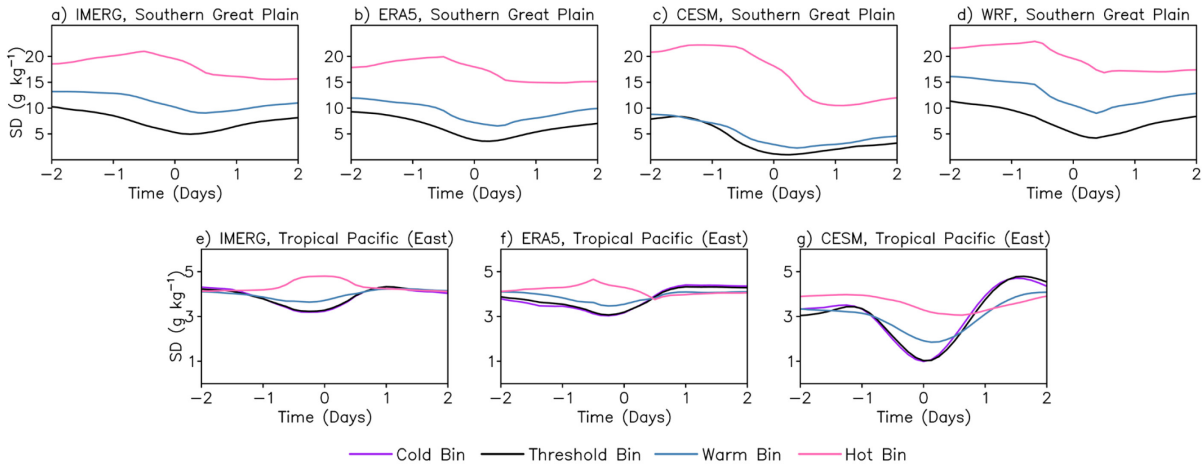

574

575 **Figure 11.** Evolution of near-surface saturation deficit, using two sample areas in the U.S.
576 Southern Great Plain (top) and Tropical Pacific (East) (bottom) as land and ocean examples.
577 Time series of near-surface saturation deficit (g kg^{-1}) before and after the storm peak are
578 averaged among extreme events within each temperature bin, based on 3-hourly warm-season
579 data during 2001-2013 from a) and e) IMERG, b) and f) ERA5, c) and g) CESM, and (d) WRF.
580 The cold, threshold, warm and hot bins are as marked in Figure 2.

581 Results in Figures 9-11 together demonstrate the important role that saturation deficit plays
582 in shaping the relationship between temperature and extreme precipitation over land. High
583 temperature, through its impact on saturation deficit and ultimately on atmospheric convection
584 and updraft condensation rate, plays an essential role in causing the negative scaling of extreme
585 precipitation over land.

586 *d. Potential impact of large-scale systems on the negative EPI-T scaling*

587 As both temperature and precipitation respond to large-scale systems, a negative EPI-T
588 scaling at high temperature may result from anomalous large-scale conditions. In any given
589 region, for instance, near-surface air temperatures are usually high during dry spells, when
590 heatwaves are prevalent and moist convection tends to be suppressed; similarly, large-scale
591 descending motion suppresses convection (precipitation) and meanwhile induces adiabatic
592 warming of the land surface. In some regions, climatological conditions have a specific sub-
593 seasonal pattern that may cause an apparent negative scaling. Taking the U.S. Midwest as an
594 example, July and August are generally warmer than June, while the large-scale setting in June
595 is more favorable for convection and precipitation. To examine the impact of a large-scale
596 system on the EPI-T relationship through its influence on both temperature and precipitation,
597 we experiment using two additional approaches to derive the binned EPI-T scaling curves. In
598 one, we randomly sample the temperature and precipitation data in time to break continuous
599 dry spells and use only one-third of the rainy season data from each source (Figure S26). In the

other, we derive the scaling curves for each month separately to eliminate the effects of climatological sub-seasonal variations (Figure S27). Regardless of which data source we use, the results (Figures S26-S27) are all qualitatively similar to those based on all wet season data in Figure 2 (solid lines), suggesting that anomalous large-scale conditions are not the dominant cause for the overall shape (and the negative scaling) of the EPI-T relationship.

The CESM 850-hPa geopotential height (Z_{850}) anomalies (Supplementary Figures S28-S29) also show no clear cyclonic-anticyclonic contrast between the cold bin (or threshold bin) and the hot bin (or warm bin). In the warm bins, cyclonic (as opposed to anticyclonic) large-scale systems occur more frequently than the warm season mean condition over all regions, as indicated by the negative Z_{850} anomalies, except for the Amazon; in the hot bins, the negative Z_{850} anomalies persist in most regions, except for the Amazon, the U.S. Midwest, and Central Europe. Over the tropical Pacific (East and West) and tropical Atlantic, the overall impact of large-scale systems is minimal, as indicated by the correspondingly small magnitude of Z_{850} anomalies. These results, in combination with the lack of anticyclonic anomalies in the northern Atlantic and tropical Indian (Figure S29), suggest that subsidence makes limited contributions in shaping the rather homogeneous vertical profiles of saturation deficit over the ocean (Figure S18). Instead, the rather uniform vertical profile of saturation deficit might be a result of other processes, such as dry air intrusion in the middle troposphere.

These results, in combination with results from the randomized and month-specific scaling analyses, suggest that, while variations of large-scale systems may contribute to the negative EPI-T scaling at very high temperature (hot bins) in some regions, they are not the fundamental cause for the negative scaling documented in this study.

5. Conclusions and discussion

Based on analysis of the observational IMERG data, the ERA5 reanalysis product, and output from the coarse-resolution CESM and convection-permitting NCAR WRF simulations, we show that the negative scaling of extreme precipitation at high temperature is a robust feature of the precipitation-temperature relationship at the weather timescale during the warm season. Although the magnitude of extreme precipitation varies with data source and spatiotemporal resolution, the negative scaling nature of the precipitation-temperature relationship remains qualitatively the same. These statements hold over both land and ocean.

630 The primary mechanisms underlying the negative scaling differ between land and ocean.
631 We conclude that the negative scaling of warm-season precipitation extremes at high
632 temperature *over land* results primarily from the heat-induced suppression of precipitation
633 intensity. We base this conclusion on the concurrent and lead-lag relationships between
634 temperature and extreme precipitation, and on the temporal evolution of temperature and
635 saturation deficit during heavy storm events. Precipitation cooling and cloud radiative effects
636 play a secondary role in the negative scaling over land, but are more fundamental over oceans.
637 Over land, temperature and saturation deficit differences between extreme precipitation events
638 are already in place prior to the development of the storms; over oceans, such differences
639 emerge during the development and occurrence of the storms. These conclusions, as well as
640 the robustness of negative scaling at high temperature, remain unchanged when the analysis is
641 based on alternative data versions, TRMM 3B42 and ERA-Interim (results not shown).

642 At the process level and at the weather scale, results from CESM diagnostics indicate that
643 high temperature reduces precipitation intensity through the suppression of convective updraft
644 condensation rate and the acceleration of condensate evaporation, both due to increased
645 saturation deficit over land at high temperature. Over oceans, both the saturation deficit and its
646 range of variation are small and have limited impact on convection and precipitation. Instead,
647 the large contrast in extreme precipitation over a small range of saturation deficit over the ocean
648 is a reflection of saturation deficit responding to evaporation of precipitation. To examine the
649 robustness of this conclusion and its potential model dependence, one could repeat the
650 convection-related diagnostics using output from the NCAR WRF convection-permitting
651 simulation, but some variables needed for such analysis are not available from the fine-
652 resolution NCAR WRF model output (or similarly from ERA5 either). Nevertheless, the
653 consistency between the diagnosed cumulus downdraft evaporation rate (Figure 8) and the
654 DCAPE (Figure S17) lends certain confidence to our CESM-based process analysis.

655 The local processes shaping the relationship between extreme precipitation and temperature
656 are always under the influence of large-scale systems. Large-scale weather systems (that persist
657 for weeks or longer) may influence both precipitation and temperature, leading to an apparent
658 negative scaling of extreme precipitation with temperature even in the absence of a causal-
659 effect relationship between the two. Results from both the randomized analysis (that reduces
660 the large-scale effects) and the month-specific analysis (that limits data to those under the
661 climatologically same or similar synoptic settings) suggest that large-scale systems are likely

not a fundamental cause for the negative scaling. The analysis of 850-hPa geopotential height anomalies during heavy storms in different temperature bins supports a similar conclusion. With the influence of large-scale systems, the precipitation-temperature relationship and its characteristics (e.g., the threshold temperature) may change quantitatively, but would likely remain qualitatively similar.

While this study focuses on the intensity of heavy precipitation, binned analysis on mean precipitation intensity (MPI, Figure 12) and number of rainy days (not shown) indicates that precipitation amount and frequency follow a similar scaling behavior with temperature, although the corresponding threshold temperatures differ. At the event level, precipitation duration, spatial coverage, and spatiotemporal distribution are important characteristics that may confound the precipitation scaling relationship with temperature. Long et al. (2021) based on station data found that rain events under high temperature tend to be more concentrated in space and time, which would favor more intense precipitation over a short duration or over a small area. Therefore, using data with a spatiotemporal resolution much finer than available to the current study may alleviate the negative scaling. Visser et al. (2021) found that negative scaling can be eliminated if the intensity scaling analysis is conditioned on short rain duration. On the other hand, even at spatiotemporal resolutions as coarse as used in the current study, Wang and Sun (2022) found a monotonic increase of extreme precipitation intensity with temperature when the scaling analysis was conditioned on saturated atmosphere, consistent with the important role of saturation deficit proposed in this study. However, as rain duration cannot be reliably derived from coarse resolution gridded data, a comparison between the roles of rain duration and saturation deficit is beyond the scope of this study and will be tackled in follow-up research.

In the context of climate variability, temperature is not the only predictor for precipitation characteristics. Many other factors are at play and confound the scaling of precipitation with temperature, and soil moisture is one such factor. Closely coupled with local temperature, soil moisture influences precipitation processes through positive or negative feedbacks, depending on temporal and spatial scales (e.g., Barros and Hwu 2002; Findell and Eltahir 2003; Kim and Wang 2007; Koster et al. 2011; Mei and Wang 2011; Taylor et al. 2012). Functioning as an additional moisture source for the atmosphere, wetter soil enhances evapotranspiration and increases atmospheric moisture content, thus reducing saturation deficit. This may alleviate the negative scaling and shift the threshold temperature toward higher values. Another important

confounding factor is aerosol, through its direct effect on surface radiative budget (therefore temperature) and indirect effect on clouds (therefore precipitation) (e.g., Stevens and Feingold 2009; Tao et al. 2012; Rosenfeld et al. 2014; Khain et al. 2015; Da Silva et al. 2020). Specifically, Da Silva et al. (2020) showed that, due to the indirect effect of aerosols, high aerosol concentrations tend to suppress convective precipitation at low temperatures, leading to a super-CC scaling rate on the increasing branch of the EPI-T scaling curves. This effect, however, is likely not fundamental to the negative scaling at high temperature when clouds tend to be less frequent (Figures S11-S12). In fact, negative scaling is captured in the CESM simulation that prescribes aerosol concentrations (Section 2).

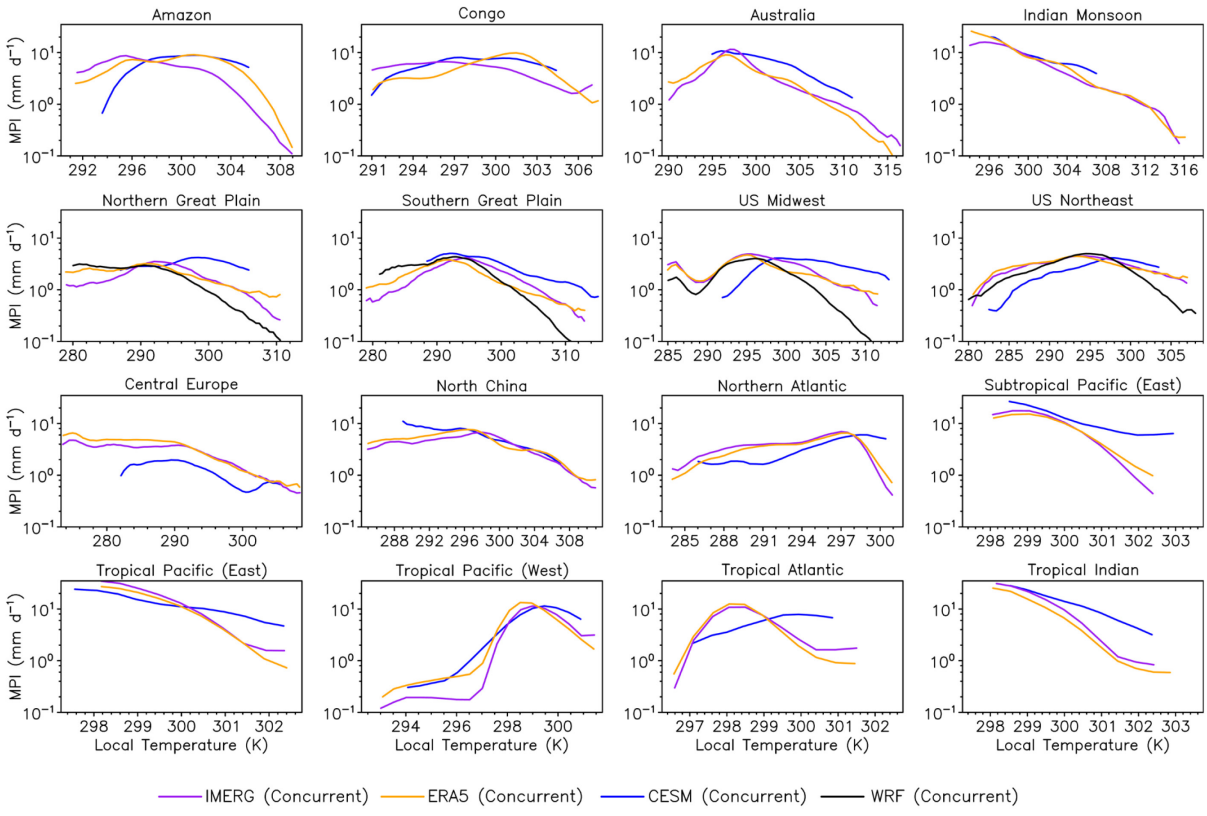

Figure 12. The MPI-T scaling relationship that links mean precipitation intensity to concurrent near-surface air temperature for 16 sample areas. The analyses are based on 3-hourly data from IMERG, ERA5, CESM, and WRF during the 2001-2013 warm seasons, with temperature in K and MPI in mm day^{-1}.

Findings from this study have significant implications concerning the understanding of extreme events such as flood, drought, and heatwaves and for projecting their future changes. In a warmer climate, Wang et al. (2017) and Drobinski et al. (2018) found that the peak-shaped extreme precipitation-temperature scaling curve, especially for its increasing branch, would shift upward and rightward (Figure 1), with increases predicted in both the peak of extreme

precipitation and the threshold temperature at which the precipitation peaks. In fact, numerous studies have shown evidence from both modeling and observational perspectives for an increase in precipitation extremes with global warming, leading to increased flood risks (e.g., Allan and Soden 2008; Fischer and Kutti 2016; Prein et al. 2017; Wang et al. 2020; Wang & Sun, 2022). As warming continues, because the rate of warming is faster over land than over oceans and much of the moisture over land originates from oceans, the atmospheric relative humidity is expected to decrease and the saturation deficit to increase over land (Sherwood and Fu 2014). Based on results from our study, this increased saturation deficit may lead to more widespread negative scaling of precipitation intensity with temperature, which provides a theoretical basis for the model-projected increase in the spatial extent of negative scaling (Wang et al. 2017).Because negative scaling occurs for both the extremes (Figure 2) and mean precipitation (Figure 12), this also means the combination of high temperature with low or lack of precipitation may become more prevalent, leading to increased co-occurrence of drought and heatwaves (Mazdiyasni and AghaKouchak 2015; Zscheischler and Seneviratne 2017), another important consequence of climate change for which this study offers a possible explanation.

Acknowledgments

We thank NASA, NCAR and ECMWF for making their datasets available. Computing resources and data storages were provided by the NCAR Computational and Information Systems Laboratory (CISL). This research was funded by the National Science Foundation (NSF) under Grant AGS-1659953. We thank three anonymous reviewers for their comments and suggestions. The authors declare no competing financial interests.

Data Availability Statement

TRMM 3B42 and IMERG are available from the NASA website at https://disc.gsfc.nasa.gov/datasets/TRMM_3B42_7/summary and https://gpm.nasa.gov/data/imerg, respectively; ERA-Interim and ERA5 are available from the ECMWF website at https://www.ecmwf.int/en/forecasts/datasets/archive-datasets/reanalysis-datasets/era-interim and https://www.ecmwf.int/en/forecasts/datasets/reanalysis-datasets/era5, respectively; Output from the CESM simulation is available at https://dataverse.harvard.edu/dataset.xhtml?persistentId=doi:10.7910/DVN/BATG5H, and

the model codes are available at http://www.cesm.ucar.edu/models/cesm1.2/. Output from the high-resolution WRF simulations of North America is available from NCAR at https://rda.ucar.edu/datasets/ds612.0/.

748 REFERENCES

749 Ali, H., H. J. Fowler, and V. Mishra, 2018: Global observational evidence of strong linkage
750 between dew point temperature and precipitation extremes. *Geophys. Res. Lett.,* **45,** 12,320-
751 12,330.

752 Allan, R. P., and B. J. Soden, 2008: Atmospheric warming and the amplification of
753 precipitation extremes. *Science,* **321,** 1481-1484.

754 Bao, J., S. C. Sherwood, L. V. Alexander, and J. P. Evans, 2017: Future increases in extreme
755 precipitation exceed observed scaling rates. *Nat. Clim. Change,* **7,** 128-132.

756 Bao, J., S. C. Sherwood, L. V. Alexander, and J. P. Evans, 2018: Comments on "temperature-
757 extreme precipitation scaling: A two-way causality?". *Int. J. Climatol.,* **38,** 4661-4663.

758 Barbero, R., S. Westra, G. Lenderink, and H. J. Fowler, 2018: Temperature-extreme
759 precipitation scaling: a two-way causality? *Int. J. Climatol.,* **38,** e1274-e1279.

760 Barros, A. P., and W. Hwu, 2002: A study of land-atmosphere interactions during summertime
761 rainfall using a mesoscale model. *J. Geophys. Res. Atmos.,* **107,** 4227,
762 doi:10.1029/2000JD000254.

763 Berg, P., C. Moseley, and J. O. Haerter, 2013: Strong increase in convective precipitation in
764 response to higher temperatures. *Nat. Geosci.,* **6,** 181-185.

765 Brown, R., and C. Zhang, 1997: Variability of midtropospheric moisture and its effect on
766 cloud-top height distribution during TOGA COARE. *J. Atmos. Sci.,* **54,** 2760-2774.

767 Byrne, M. P., and P. A.O'Gorman, 2018: Trends in continental temperature and humidity
768 directly linked to ocean warming. *Proc. Natl. Acad. Sci. USA,* **115,** 4863-4868.

769 Chan, S. C., E. J. Kendon, N. M. Roberts, H. J. Fowler, and S. Blenkinsop, 2016: Downturn in
770 scaling of UK extreme rainfall with temperature for future hottest days. *Nat. Geosci.,* **9,** 24-
771 28.

772 Chen, G., Y. Ming, N. D. Singer, and J. Lu, 2011: Testing the Clausius-Clapeyron constraint
773 on the aerosol-induced changes in mean and extreme precipitation. *Geophys. Res. Lett.,* **38,**
774 L04807.

775 Da Silva, N., S. Mailler, and P. Drobinski, 2020: Aerosol indirect effects on the temperature-
776 precipitation scaling. *Atmos. Chem. Phys.,* **20,** 6207-6223.

777 Dai, N., and Soden, B. J., 2020, Convective aggregation and the amplification of tropical
778 precipitation extremes. *AGU Adv.,* **1,** e2020AV000201.

779 Dee, D. P., S. M. Uppala, A. J. Simmons, P. Berrisford, P. Poli, et al., 2011: The ERA-Interim
780 reanalysis: configuration and performance of the data assimilation system. *Q. J. R.*
781 *Meteorol. Soc.,* **137,** 553-597.

782 Derbyshire, S. H., I. Beau, P. Bechtold, J.-Y. Grandpeix, J.-M. Piriou, J.-L. Redelsperger, and
783 P. M. M. Soares, 2004: Sensitivity of moist convection to environmental humidity. *Q. J. R.*
784 *Meteorol. Soc.,* **130,** 3055-3079.

785 Drobinski, P., B. Alonzo, S. Bastin, N. Da Silva, and C. J. Muller, 2016: Scaling of
786 precipitation extremes with temperature in the French Mediterranean region: what explains
787 the hook shape? *J. Geophys. Res. Atmos.,* **121,** 3100-3119.

788 Drobinski, P., and Coauthors, 2018: Scaling precipitation extremes with temperature in the
789 Mediterranean: Past climate assessment and projection in anthropogenic scenarios. *Climate*
790 *Dyn.,* **51,** 1237-1257.

791 Easterling, D.R., Kunkel, K.E., Arnold, J.R., et al., 2017: Precipitation change in the United
792 States. In: Climate Science Special Report:Fourth National Climate Assessment, Volume
793 I. Wuebbles, D.J., D.W. Fahey, K.A. Hibbard, D.J. Dokken, B.C. (eds.). U.S. Global
794 Change Research Program, Washington DC, pp. 207-230.

795 Emanuel, K. A., Atmospheric Convection (Oxford Univ. Press, New York, 1994).

796 Findell, K. L., and E. A. B. Eltahir, 2003: Atmospheric controls on soil moisture-boundary
797 layer interactions. Part II: Feedbacks within the continental United States. *J.*
798 *Hydrometeorol.,* **4,** 570-583.

799 Fischer, E. M., and R. Kutti, 2016: Observed heavy precipitation increase confirms theory and
800 early models. *Nat. Clim. Change,* **6,** 986-991.

801 Fowler, H. J., and Coauthors, 2021: Anthropogenic intensification of short-duration rainfall
802 extremes. *Nat. Rev. Earth Environ.,* **2,** 107-122.

803 Hardwick Jones, R., S. Westra, and A. Sharma, 2010: Observed relationships between extreme
804 sub-daily precipitation, surface temperature, and relative humidity. *Geophys. Res. Lett.,* **37,**
805 L22805.

Hersbach, H., and Coauthors, 2020: The ERA5 global reanalysis. *Quart. J. Roy. Meteor. Soc.,* **146,** 1999-2049.

Houze, R. A. Jr., C. Cheng, C. A. Leary, and J. F. Gamache, 1980: Diagnosis of cloud mass and heat fluxes from radar and synoptic data. *J. Atmos. Sci.,* **37,** 754-773.

Huffman, G. J., D. T. Bolvin, E. J. Nelkin, D. B. Wolff, R. F. Adler, G. Gu, Y. Hong, K. P. Bowman, and E. F. Stocker, 2007: The TRMM multisatellite precipitation analysis (TMPA): Quasi-global, multiyear, combined-sensor precipitation estimates at fine scales. *J. Hydrometeorol.,* **8,** 38-55.

Huffman, G. J., E. F. Stocker, D. T. Bolvin, E. J. Nelkin, and J. Tan, 2019: GPM IMERG Final Precipitation L3 Half Hourly 0.1 degree × 0.1 degree V06. Goddard Earth Sciences Data and Information Services Center, accessed 1 September 2021, https://doi.org/10.5067/GPM/IMERG/3B-HH/06.

Hurrell, J., J. Hack, D. Shea, J. Caron, and J. Rosinski, 2008: A new sea surface temperature and sea ice boundary data set for the Community Atmosphere Model. *J. Clim.,* **21,** 5145-5153.

Khain, A. P., K. D. Beheng, A. Heymsfield, A. Korolev, S. O. Krichak, Z. Levin, M. Pinsky, V. Phillips, T. Prabhakaran, A. Teller, S. C. van den Heever, and J.-I. Yano, 2015: Representation of microphysical processes in cloud resolving models: Spectral (bin) microphysics versus bulk parameterization. *Rev. Geophys.,* **53,** 247-322.

Kharin, V.V., G. M. Flato, X. Zhang, N. P. Gillett, F. Zwier, and K. J. Anderson, 2018: Risks from climate extremes change differently from 1.5°C to 2.0°C depending on rarity. *Earth's Future,* **6,** 704-715.

Kim, Y. J., and G. Wang, 2007: Impact of initial soil moisture anomalies on subsequent precipitation over North America in the coupled land-atmosphere model CAM3-CLM3. *J. Hydrometeorol.,* **8,** 534-550.

Koster, R. D., S. P. P. Mahanama, T. J. Yamada, G. Balsamo, A. A. Berg, M. Boisserie, P. A. Dirmeyer, F. J. Doblas-Reyes, G. Drewitt, C. T. Gordon, Z. Guo, J.-H. Jeong, W.-S. Lee, Z. Li, L. Luo, S. Malyshev, W. J. Merryfield, S. I. Seneviratne, T. Stanelle, B. J. J. M. van den Hurk, F. Vitart, and E. F. Wood, 2011: The second phase of the global land atmosphere coupling experiment: Soil moisture contribution to subseasonal forecast skill. *J. Hydrometeorol.,* **12,** 805-822.

837 Lenderink, G., and E. van Meijgaard, 2008: Increase in hourly precipitation extremes beyond
838 expectations from temperature changes. *Nat. Geosci.,* **1,** 511-514.

839 Liu, C., K. Ikeda, R. Rasmussen, M. Barlage, A. J. Newman, A. F. Prein, F. Chen, L. Chen, M.
840 Clark, A. Dai, J. Dudhia, T. Eidhammer, D. Gochis, E. Gutmann, S. Kurkute, Y. Li, G.
841 Thompson, and D. Yates, 2017: Continental-scale convection-permitting modeling of the
842 current and future climate of North America. *Clim. Dyn.,* **49,** 71-95.

843 Long, K., D. Wang, G. Wang, J. Zhu, S. Wang, 2021: High temperature enhances spatio-
844 temporal rainfall concentration. *Journal of Hydrometeorology*,
845 https://doi.org/10.1175/JHM-D-21-0034.1

846 Loriaux, J. M., G. Lenderink, S. R. De Roode, and A. P. Siebesma, 2013: Understanding
847 convective extreme precipitation scaling using observations and an entraining plume
848 model. *J. Atmos. Sci.,* **70,** 3641-3655.

849 Mazdiyasni, O., and A. AghaKouchak, 2015: Substantial increase in concurrent droughts and
850 heatwaves in the United States. *Proc. Natl Acad. Sci. USA,* **112,** 11484-11489.

851 Meehl, G. A., T. F. Stocker, W. D. Collins, P. Friedlingstein, A. T. Gaye, J. M. Gregory, A.
852 Kitoh, R. Knutti, J. M. Murphy, A. Noda, S. C. B. Raper, I. G. Watterson, A. J. Weaver,
853 and Z. C. Zhao, Global Climate Projections. In Climate Change (2007), The Physical
854 Science Basis. Contribution of Working Group I to the Fourth Assessment Report of the
855 Intergovernmental Panel on Climate Change (eds S. Solomon, D. Qin, M. Manning, Z.
856 Chen, M. Marquis, K. B. Averyt, M. Tignor, H. L. Miller) (Cambridge University Press,
857 Cambridge, UK, 2007).

858 Mei, R., and G. Wang, 2011: Impact of sea surface temperature and soil moisture on summer
859 precipitation in the United States based on observational data. *J. Hydrometeorol.,* **12,** 1086-
860 1099.

861 Mishra, V., J. M. Wallace, and D. P. Lettenmaier, 2012: Relationship between hourly extreme
862 precipitation and local air temperature in the United States. *Geophys. Res. Lett.,* **39,**
863 L16403.

864 Muller, C., 2013: Impact of convective organization on the response of tropical precipitation
865 extremes to warming. *J. Clim.,* **26,** 5028-5043.

866 Neale, R. B., A. Gettelman, S. Park, C.-C. Chen, P. H. Lauritzen, D. L. Williamson, A. J.
867 Conley, D. Kinnison, D. Marsh, A. K. Smith, F. Vitt, R. Garcia, J.-F. Lamarque, M. Mills,
868 S. Tilmes, H. Morrison, P. Cameron-Smith, W. D. Collins, M. J. Iacono, R. C. Easter, X.
869 Liu, S. J. Ghan, P. J. Rasch, and M. A. Taylor, Description of the NCAR Community
870 Atmosphere Model (CAM 5.0). Tech. Report NCAR/TN-486+STR (National Center for
871 Atmospheric Research, 2012).

872 O'Gorman, P. A., and T. Schneider, 2009: The physical basis for increases in precipitation
873 extremes in simulations of 21st-century climate change. *Proc. Natl Acad. Sci. USA,* **106,**
874 14773-14777.

875 O'Gorman, P. A., 2015: Precipitation extremes under climate change. *Curr. Clim. Change Rep.,*
876 **1,** 49-59.

877 Oleson, K. W., D. M. Lawrence, G. B. Bonan, B. Drewniak, M. Huang, C. D. Koven, S. Levis,
878 F. Li, W. J. Riley, Z. M. Subin, S. C. Swenson, P. E. Thornton, A. Bozbiyik, R. Fisher, C.
879 L. Heald, E. Kluzek, J.-F. Lamarque, P. Lawrence, L. R. Leung, W. Lipscomb, S. Muszala,
880 D. M. Ricciuto, W. Sacks, Y. Sun, J. Tang, and Z.-L. Yang, Technical description of
881 version 4.5 of the Community Land Model (CLM). NCAR Technical Note NCAR/TN-
882 503+STR (National Center for Atmospheric Research, 2013).

883 Prein, A. F., R. M. Rasmussen, K. Ikeda, C. Liu, M. P. Clark, and G. J. Holland, 2017: The
884 future intensification of hourly precipitation extremes. *Nat. Clim. Change,* **7,** 48-52.

885 Rasmussen, R., and C. Liu. 2017. High Resolution WRF Simulations of the Current and Future
886 Climate of North America. Research Data Archive at the National Center for Atmospheric
887 Research, Computational and Information Systems Laboratory.
888 https://doi.org/10.5065/D6V40SXP. Accessed March 15, 2018.

889 Redelsperger, J., D. Parsons, and F. Guichard, 2002: Recovery processes and factors limiting
890 cloud-top height following the arrival of a dry intrusion observed during TOGA COARE.
891 *J. Atmos. Sci.,* **59,** 2438-2457.

892 Roderick, T. P., C. Wasko, and A. Sharma, 2019: Atmospheric moisture measurements explain
893 increases in tropical rainfall extremes. *Geophys. Res. Lett.,* **46,** 1375-1382.

894 Romps, D. M., 2010: A direct measurement of entrainment, *J. Atmos. Sci.,* **67,** 1908-1927.

895 Rosenfeld, D., M. O. Andreae, A. Asmi, M. Chin, G. de Leeuw, D. P. Donovan, R. Kahn, S.
896 Kinne, N. Kivekäs, M. Kulmala, W. Lau, K. S. Schmidt, T. Suni, T. Wagner, M. Wild, and
897 J. Quaas, 2014: Global observations of aerosol-cloud-precipitation-climate interactions.
898 *Rev. Geophys.,* **52,** 750-808.

899 Sherwood, S. C., and Q. Fu, 2014: A drier future? *Science,* **343,** 737-739.

900 Singh, M. S., and P. A. O'Gorman, 2014: Influence of microphysics on the scaling of
901 precipitation extremes with temperature. *Geophys. Res. Lett.,* **41,** 6037-6044.

902 Skamarock, W. C., J. B. Klemp, J. Dudhia, D. O. Gill, D. M. Barker, M. G. Duda, X. Huang,
903 W. Wang, and J. G. Powers, A Description of the Advanced Research WRF Version 3.
904 NCAR Technical Note NCAR/TN-475+STR (National Center for Atmospheric Research,
905 2008).

906 Stevens, B., and G. Feingold, 2009: Untangling aerosol effects on clouds and precipitation in
907 a buffered system. *Nature,* **461,** 607-613.

908 Sugiyama, M., H. Shiogama, and S. Emori, 2009: Precipitation extreme changes exceeding
909 moisture content increases in miroc and ipcc climate models. *Proc. Natl Acad. Sci. USA,*
910 **107,** 571-575.

911 Takayabu, Y. N., S. Shige, W.-K. Tao, and N. Hirota, 2010: Shallow and deep latent heating
912 modes over tropical oceans observed with TRMM spectral latent heating data. *J. Clim.,* **23,**
913 2030-2046.

914 Tao, W.-K., J.-P. Chen, Z. Li, C. Wang, and C. Zhang, 2012: Impact of aerosols on convective
915 clouds and precipitation. *Rev. Geophys.,* **50,** RG2001, doi:10.1029/2011RG000369.

916 Taylor, C. M., R. A. M. de Jeu, F. Guichard, P. P. Harris, and W. A. Dorigo, 2012: Afternoon
917 rain more likely over drier soils. *Nature,* **489,** 423-426.

918 Trenberth, K. E., 1999: Conceptual framework for changes of extremes of the hydrologic cycle
919 with climate change. *Climatic Change,* **42,** 327-339.

920 Trenberth, K. E., and D. J. Shea, 2005: Relationships between precipitation and surface
921 temperature. *Geophys. Res. Lett.,* **32,** L14703, https://doi.org/10.1029/2005GL022760.

922 Utsumi, N., S. Seto, S. Kanae, E. E. Maeda, and T. Oki, 2011: Does higher surface temperature
923 intensify extreme precipitation? *Geophys. Res. Lett.,* **38,** L16708.

924 Visser, J. B., Wasko, C., Sharma, A., & Nathan, R., 2021: Eliminating the "Hook" in
925 Precipitation-Temperature Scaling, Journal of Climate, **34**(23), 9535-9549.

926 Wang, G., D. Wang, K. E. Trenberth, A. Erfanian, M. Yu, M. G. Bosilovich, and D. T. Parr,
927 2017: The peak structure and future changes of the relationships between extreme
928 precipitation and temperature. *Nat. Clim. Change,* **7,** 268-274.

929 Wang, G., C. J. Kirchhoff, A. Seth, J. T. Abatzoglou , B. Livneh, D. W. Pierce, L. Fomenko,
930 and T. Ding, 2020: Projected changes of precipitation characteristics depend on
931 downscaling method and the training data: LOCA vs. MACA using the U.S. Northeast as
932 an example. *J. Hydrometeorol.,* doi:10.1175/JHM-D-19-0275.1.

933 Wang, G., and X. Sun, 2022: Monotonic increase of extreme precipitation intensity with
934 temperature when controlled for saturation deficit. *Geophys. Res. Lett.,* 49, e2022GL097881

935 Wasko, C., A. Sharma, and F. Johnson, 2015: Does storm duration modulate the extreme
936 precipitation temperature scaling relationship? *Geophys. Res. Lett.,* **42,** 8783-8790.

937 Zhang, G. J., and N. A. McFarlane, 1995: Sensitivity of climate simulations to the
938 parameterization of cumulus convection in the Canadian Climate Center general-
939 circulation model. *Atmos. Ocean,* **33,** 407-446.

940 Zhang, K., R. Fu, M. J. Shaikh, S. Ghan, M. Wang, L. R. Leung, R. E. Dickinson, and J.
941 Marengo, 2017: Influence of super-parameterization and a higher-order turbulence closure
942 on rainfall bias over Amazonia in community atmosphere model version 5 (CAM5). *J.*
943 *Geophys. Res.,* **122,** 9879-9902.

944 Zscheischler, J., and S. I. Seneviratne, 2017: Dependence of drivers affects risks associated
945 with compound events. *Sci. Adv.,* **3,** e1700263.